Self-organization of SiGe planar nanowires via anisotropic elastic field

Kailang Liu, Isabelle Berbezier,* Luc Favre, Antoine Ronda, Thomas David, and Marco Abbarchi
Institut Matériaux Microélectronique Nanoscience de Provence, Aix-Marseille Université, UMR CNRS 6242, 13997 Marseille, France†

Philippe Gaillard and Thomas Frisch
Université Côte d'Azur, CNRS, Institut de Physique de Nice, Parc Valrose, 06108 Nice, France

Bernard Croset and Jean-Noël Aqua‡
Sorbonne Université, CNRS, Institut des Nanosciences de Paris, INSP, UMR 7588, 4 place Jussieu, 75005 Paris, France

(Received 10 July 2018; published 12 February 2019)

Strained epitaxial SiGe on vicinal Si(001) substrates develops a morphological instability perpendicular to the steps unlike the usual growth instabilities on vicinal substrates, eventually leading to planar nanowires. We assess both theoretically and experimentally the effect of strain anisotropy on the 1D elongation of the Asaro-Tiller-Grinfel'd (ATG) instability. The anisotropy of strain relaxation due to the presence of step edges is considered in a continuum model with two different effective strains in the surface plane. We show that the measured in-plane strain anisotropy and the theoretical model are consistent with the experimental morphologies. Nice network of ultrasmall aligned elongations are predicted resulting from a complex interplay of kinetic and energetic phenomena associated with strain anisotropy.

DOI: 10.1103/PhysRevMaterials.3.023403

I. INTRODUCTION

Growth of self-organised SiGe islands has been studied for a long time both as a model system [1–8] and because of their huge potential applications in band-gap engineering based optoelectronic devices [9–14]. At present, because of the poor reliability of the quantum dots (QDs) self-organization process, most of the devices under investigation use strain-induced band-gap engineering based on 2D SiGe films [15–17]. In the past ten years, it was demonstrated that the use of 1D nanowires (NWs) instead of quantum dots could be of great interest for anisotropic electronic transport and 2D quantum confinement effects [18–20]. They are now easily integrated in 1D gate transistors and constitute an alternative way to produce more efficient devices [21–24]. One major hurdle to overcome in order to allow their introduction in microelectronic devices is the presence of metallic catalysts present not only on the tip of the nanowires but all along their sides. For this reason, several complex nanolithographic processes have been developed for the fabrication of new and especially planar NWs [25–27]. However, their size is to large to provide 2D quantum confinement effects as predicted by theory [28]. Growth of self-organized homogeneous, dense and small planar 1D islands would be a simple and versatile method for the integration of nanowires in devices. A few studies demonstrated that the deposition of Ge on vicinal substrates can result in nanowires with lengths $>1\ \mu$m under optimized conditions [29–31]. Persichetti *et al.* [30] suggested that a 3D to 1D shape transformation results from anisotropic elastic interactions on vicinal substrates. For lower strained SiGe layers, similar elongation was observed in the Asaro-Tiller-Grinfel'd (ATG) instability regime [32,33]. However, a fundamental question raised is how such 1D elongation proceeds and its variance with the ATG instability on nominal substrates.

We examine here the effect of the substrate misorientation on the morphologies produced in the low-strain regime [34–36]. We measure and analyze by x-ray diffraction the strain relaxation of SiGe films deposited on nominal Si(001) and vicinal 10° off substrate. By comparison of the Poisson dilatation, we characterize the asymmetry of the in-plane strain relaxation on the vicinal substrate. In this case, the system evolves into 1D ripples perpendicular to the steps, which eventually lead to planar nanowires. To rationalize this evolution, we introduce anisotropic misfits reflecting the strain anisotropy measured experimentally, in a dynamical model of surface diffusion. It depicts well the experimental finding, with an instability growing perpendicularly to the steps that has a good geometrical characteristics compared to experiments.

II. GROWTH

$Si_{1-x}Ge_x$ thin films were deposited by molecular beam epitaxy (MBE) on top of nominal and vicinal Si(001) substrates disoriented from 0.1° to 10° off in the ⟨110⟩ direction. The samples are loaded in the MBE machine after an ex situ chemical cleaning process, which follows a modified Shiraki recipe: (i) 10 min in HNO_3 (65%) heated at 70 °C, (ii) 1 min in deionized water, and (iii) 30 s in HF (49%):H_2O (1:10).

*isabelle.berbezier@im2np.fr
†Present address: Institut des Nanosciences de Paris, Sorbonne Université and CNRS UMR 7588, 4 place Jussieu, 75252 Paris, France.
‡aqua@insp.jussieu.fr

 ©2019 American Physical Society

To avoid contamination, the substrates are immediately transferred under clean room atmosphere into a UHV MBE growth chamber RIBER MBE32 at the end of the chemical cleaning. The samples are then thermally cleaned *in situ* at temperatures ∼1000 °C for 2 min before growth. They are then capped by a thin 20-nm Si buffer layer, which reproduces the regular stepped surface and guarantees a flat and reliable top surface. The root mean square roughness obtained after the buffer layer growth is similar to those of Si(001) and representative of AFM electronic noise (RMS roughness 0.1 nm).

The *in situ* cleaning process is followed by epitaxial growth of $Si_{1-x}Ge_x$ layers of different thickness and composition using solid source MBE with a background pressure in the 10^{-11} Torr range. Si is evaporated from an electron gun evaporator and Ge is evaporated from an effusion cell. Beam flux and $Si_{1-x}Ge_x$ compositions are calibrated *in situ* by reflection high-energy electron diffraction oscillations. Typical $Si_{1-x}Ge_x$ growth rate is 0.027 nm/s. The Si buffer layer is deposited at 700 °C, while $Si_{1-x}Ge_x$ layers are deposited at 550 °C. After fabrication, the samples are observed by atomic force microscopy (AFM), using a PSIA XE-100. AFM is used in noncontact operating mode in air, with a NCHR-50 tip model for very high-resolution imaging, with a typical radius of about 8 nm. Atomic details on the structures are obtained by transmission electron microscopy (TEM) using a FEI Tecnai G2 and a FEI Titan 80-300 with Cs corrector. Cross-section samples are prepared using a dual-beam FIB HELIOS 600 nanolab or tripod polishing followed by PIPS thinning. TEM cross-section observations have been performed on a specially very thin part of the undulated SiGe layer (thickness 3 nm at maximum of the undulation). The main reason for this choice, is that the quality of the HR images is much better when the deposited layer is thinner. Plane view samples are prepared by mechanical and chemical polishing.

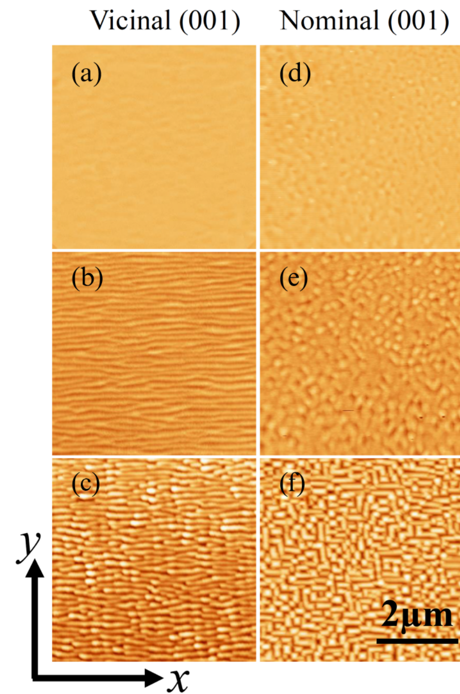

FIG. 1. AFM images of $Si_{1-x}Ge_x$ layers with (a)–(d) $h_{SiGe} = 50$, (b)–(e) 80, and (c)–(f) 100 nm. The images height scale is kept constant at 20 nm.

III. MORPHOLOGIES

Systematic experiments were done to quantify the effect of steps edges on the morphological evolution. We deposited $Si_{1-x}Ge_x$ films with $x = 0.23$ on nominal Si(001) and vicinal 10° off substrates. The thickness of the films was varied in between 50 and 150 nm. After deposition of 50 nm, Figs. 1(a)–1(d), the surfaces are flat with a RMS roughness of 0.1 nm similar to the clean Si substrates. For increasing thickness, $h_{SiGe} = 80$ nm, the instability develops and forms array of quasi 1D ripples on the vicinal substrate, while typical isotropic ATG undulations [6] develop in the nominal case, Figs. 1(b)–1(e). After deposition of $h_{SiGe} = 100$ nm, the instability breaks up into islands on both substrates.

We determined the geometry of the ripples of the vicinal case, and especially the direction of the elongation as compared to the step edges. The steps are supposed to be parallel to the y direction, while x is the in-plane perpendicular direction, Fig. 2. We performed TEM images, which clearly show that the corrugation lies over the train of steps with their longitudinal length perpendicular to the step edges, Fig. 2. The quasi-1D shape of these morphologies is well visible on large scale TEM images, Fig. 2(c). To better characterize this elongation, we deposited films on substrates with different misorientation angles in between 0.1° and 10°, and also with different Ge concentration. When varying the Ge concentration, we find that on both substrates the instability amplitude/wavelength follow the same evolution as already characterized [6]. When varying the misorientation angle at constant

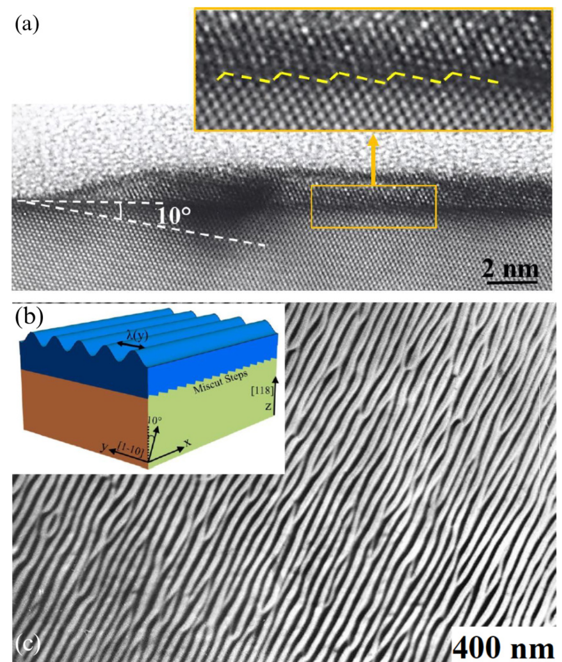

FIG. 2. (a) TEM cross-section images of an elongated corrugation on a 10° off substrate for $h_{SiGe} = 10$ nm and $x = 0.3$; (b) schematics of the undulation/steps geometry; (c) large-scale TEM plane view image of the 1D instability.

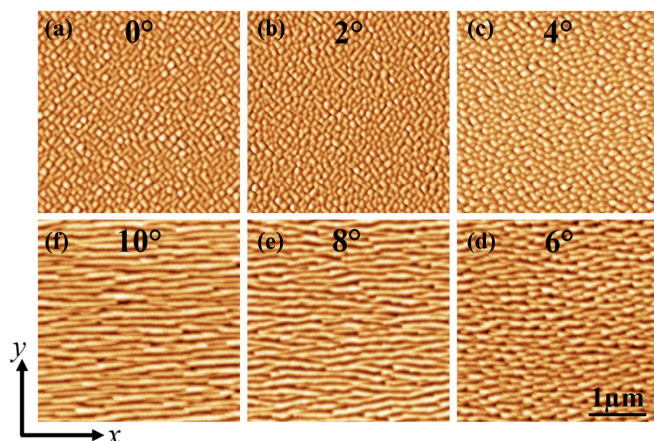

FIG. 3. Morphological evolution of the instability with the misorientation angle: AFM images of the $Si_{1-x}Ge_x$ layers for a misorientation angle equal to 0°, 2°, 4°, 6°, 8°, and 10° from (a) to (f) while $x=0.3$.

Ge concentration, the ripple mean elongation perpendicular to the steps increases when the miscut angle increases, see Fig. 3. This opens the possibility to eventually find corrugations and wires with tuneable dimensions and density.

IV. STRAIN ANISOTROPY

A. X-ray analysis

To characterize the strain state of the film, we have performed x-ray diffraction experiments using a SmartLab Rigaku diffractometer. Intensity maps around the (004) spot were acquired in a "ω step-$2\theta/\omega$ scan" mode and a symmetric geometry. The $K_{\alpha 1}$ radiation of a Cu-rotating anode ($\lambda = 0.154056$ nm^{-1}) was selected by the use of a double Ge(220) monochromator. These maps allow the measurement of the deformation perpendicular to the plane for the flat layers on nominal and 10° off substrates, Figs. 1(a)–1(d). We focused on the flat films to rule out the relaxation induced by the morphological evolution. For the nominal substrate, two peaks are observed on the map intensity of the (004) spot, Fig. 4(a), one very intense from the bulk and another weaker one from the layer. Secondary oscillations are also observed between these two peaks in the q_z direction, associated to the well-defined thickness of the layer. A cross-section profile at the maximum of intensity for the substrate averaged over 10 pixels shows that the distance between the two spots is $\delta q = 0.79$ nm^{-1}, Fig. 4(b), which gives a strain of $e_{zz}^{\mathrm{nom}} = \delta q/q_{004} = 1.70\%$. The distance between minima of the oscillations is $\delta q_z = 0.14$ nm^{-1} that corresponds to a thickness of 46 nm. This result fits well with the SiGe deposited thickness of 50 nm.

The (004) map of the vicinal substrate see Fig. 5 is more noisy due to the presence of a large density of steps at the substrate/film interface, about 1 monoatomic step every 1 nm. The distance between the two spots is $\delta q = 0.68$ nm^{-1}, which gives a strain of $e_{zz}^{\mathrm{vic}} = \delta q/q_{004} = 1.46\%$, lower than on the nominal substrate. Even if the secondary oscillations are much less visible, again due to the steps, the same thickness (46 nm) is measured on the filtered image. Considering the

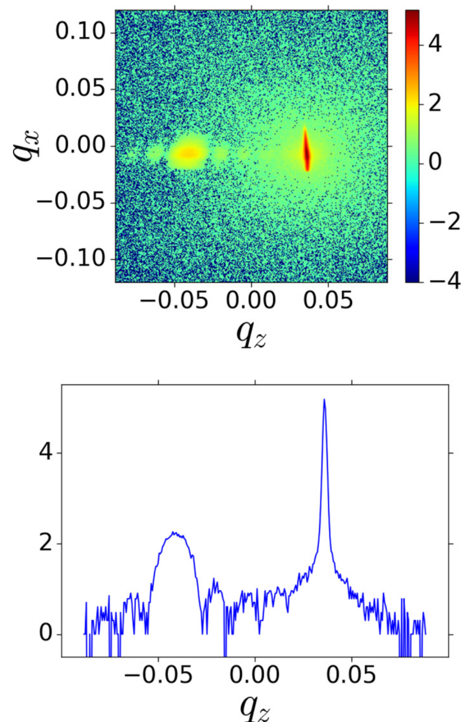

FIG. 4. (left) Map around the (004) spot for flat epilayer on a nominal (001) substrate and (right) cross-section profile for the maximum intensity.

lower q_z deformation on a vicinal substrate, we can deduce from Poisson dilatation that the $Si_{1-x}Ge_x$ film on a vicinal substrate is already partially relaxed in the plane. Such partial relaxation may be ascribed to the monoatomic steps that relax the strain perpendicular to their edges.

B. Poisson dilatation

A vicinal surface allows for a partial relaxation of the lattice-mismatch epitaxial strain. The elastic influence of the steps is both a combination of force dipoles and monopoles when the system is under stress [37–39]. We match the (a) vicinal film/substrate geometry where the film and substrate have a mismatch m in the x and y directions, with (b) an *ad hoc* geometry where the film is deposited on a plane substrate with a lattice mismatch m_y in the y direction and m_x in the x direction. We note here that $m_k = (a_k^f - a^s)/a^s$ is the

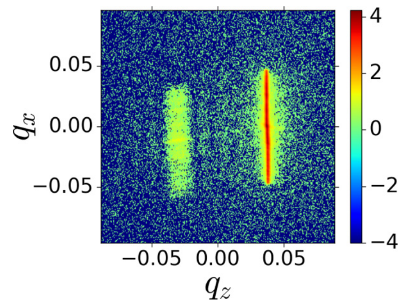

FIG. 5. Map around the (004) spot for a flat epilayer on a vicinal 10° off substrate.

lattice mismatch between the film (f) and substrate (s), which can depend on the direction k. In the geometry (b), we assume that no relaxation occurs in the y direction (the direction of the steps), so that the misfit between the film and substrate is $m_y = m$. On the other hand, the relaxation introduced by the steps is embedded in the effective mismatch m_x, which is set by comparison of the theory concerning the geometry (b) with the experimental measure of the Poisson dilatation in the geometry (a).

The Poisson dilatation is a practical measure of the strain state of a film. It can be computed within linear isotropic elasticity, with the mechanical equilibrium $\partial_j \sigma_{ij} = 0$ for $i, j = x, y, z$, where $\boldsymbol{\sigma}$ is the stress tensor, while epitaxial coherence enforces continuity of the displacement vector and normal force at the film/substrate interface, while the upper surface is supposed to be stress-free [40]. We assume equal film and substrate Young's modulus and Poisson's ratio, given the small difference in the Si and Ge parameters. In the substrate reference state, the strain is $e_{ij} = \frac{1}{2}(\partial_j u_i + \partial_i u_j) - \delta_{ij} m_k \delta_{ik} \theta(z)$, with the Heaviside function $\theta(z)$ when the film lies in the $z \geqslant 0$ region. For a flat film, mechanical equilibrium leads to the solution for the displacement vector $\boldsymbol{u}^0$,

$$\boldsymbol{u}^0 = \frac{\theta(z)}{1-\nu}[\nu\,(m_x + m_y) + (1-\nu)\,m_z]z \begin{pmatrix} 0 \\ 0 \\ 1 \end{pmatrix}, \quad (1)$$

with ν, the Poisson's ratio. In the geometry (b), the Poisson dilatation is

$$e^0_{zz} = \frac{d\boldsymbol{u}^0_z}{dz} = \frac{m_y + \nu\, m_x}{1-\nu}, \quad (2)$$

which reduces to $e^{0,\mathrm{nom}}_{zz} = m(1+\nu)/(1-\nu)$ when $m_x = m_y = m$. The experimental result on the nominal substrate e^{nom}_{zz} corresponds to this fully symmetric case $e^{0,\mathrm{nom}}_{zz}$, that leads to the nominal misfit $m = 0.96\%$. It corresponds to a film concentration $x = 0.23$ close to the expected one. For the vicinal substrate, setting $e^0_{zz} = e^{\mathrm{vic}}_{zz}$ leads to the effective misfit $m_x = 0.34\%$ if $m_y = m$. Vicinality therefore introduces a strong relaxation of the strain in the direction perpendicular to the steps, almost divided by three $m_x/m = 0.36$. We investigate in the following its influence on the subsequent evolution of the film.

V. GROWTH MODELING

A. Asymmetric strain relaxation of a corrugation

The control of the self-organization process is achieved here thanks to the inhomogeneity of the strain field [41,42]. We therefore compute the strain of a corrugated surface in presence of the asymmetry described above. Given the flat film solution $\boldsymbol{u}^0$, we compute the displacement field for a free surface with small slopes $z = h_0 + \hat{h}_1 e^{i\boldsymbol{k}\cdot\boldsymbol{r}}$, where $\boldsymbol{r} = \{x, y\}$. We solve the mechanical equilibrium in Fourier space, see e.g., Refs. [43,44], with the solution $\boldsymbol{u} = \boldsymbol{u}^0 + \boldsymbol{u}^1 + \dots$ with

$$\begin{aligned} \boldsymbol{u}^1_x(\boldsymbol{k}) = i\hat{h}_1 \frac{k_x e^{k(z-h_0)}}{k^3(1-\nu)} \big\{ & k_x^2(m_x + m_y\nu)(kz - 2\nu + 2) \\ & + k_y^2[m_x(\nu kz - 2\nu^2 + 2) + m_y kz] \\ & - kh_0\big[k_x^2(m_x + m_y\nu) + k_y^2(m_x\nu + m_y)\big]\big\}, \end{aligned} \quad (3)$$

with $k = |\boldsymbol{k}|$ and a symmetric solution for $\boldsymbol{u}_{1,y}$ where x and y are interchanged, while

$$\begin{aligned} \boldsymbol{u}^1_z(\boldsymbol{k}) = \hat{h}_1 \frac{e^{k(z-h_0)}}{k^2(1-\nu)} \big\{ & kh_0\big[k_x^2(m_x + m_y\nu) + k_y^2(m_x\nu + m_y)\big] \\ & - (kz + 2\nu - 1)\big[k_x^2(m_x + m_y\nu) + k_y^2(m_x\nu + m_y)\big]\big\}. \end{aligned} \quad (4)$$

The elastic energy density on the surface is then $\mu^{el} = \mu^{el}_0 + \mu^{el}_1$ with $\mu^{el}_0 = \mathcal{E}_0(\eta^2 + 2\eta\nu + 1)/[2(1+\nu)]$, $\mathcal{E}_0 = Y m_y^2/(1-\nu)$ and the asymmetry parameter

$$\eta = \frac{m_x}{m_y}. \quad (5)$$

The elastic chemical potential eventually reads

$$\hat{\mu}^{el}_1(\boldsymbol{k}) = -2(1+\nu)c_3(\boldsymbol{k})\,\mathcal{E}_0\,k\,\hat{h}_1, \quad (6)$$

with $k = |\boldsymbol{k}|$ and

$$\begin{aligned} c_3(\boldsymbol{k}) = \frac{1}{(1+\nu)^2 k^4}\big[& k_x^4(\eta+\nu)^2 + k_y^4(1+\eta\nu)^2 \\ & + k_x^2 k_y^2(1+\nu)(\eta^2 + 2\eta\nu + 1)\big]. \end{aligned} \quad (7)$$

B. Instability evolution

We describe the film dynamical evolution within a continuum framework appropriate to describe a nucleationless process [45]. We neglect the inhomogeneity and asymmetry introduced by the steps in the diffusion process, together with attachment-detachment issues at the steps. Consequently, we do not consider the step-bunching or step-meandering instabilities [38,46,47] that yield geometries, which can not rationalize the instability described above that grows perpendicular to the steps. We also neglect surface energy anisotropy that mainly comes into play on the long-time dynamics of the instability [36,48], together with wetting interactions irrelevant for thick films [43]. We finally also neglect a possible terrace-dependent strain anisotropy that could result from surface reconstruction differences [49]. Hence we focus on the effect of vicinality on the strain asymmetry at the origin of the morphological evolution. In the linear response framework, surface diffusion currents are proportional to gradients of the surface chemical potential μ, so that mass conservation reads

$$\partial h/\partial t = D\sqrt{1 + |\nabla h|^2}\,\boldsymbol{\Delta}_S\mu \quad (8)$$

[43,50,51], with the diffusion coefficient D and surface Laplacian $\boldsymbol{\Delta}_S$. The latter potential $\mu = \mu^s + \mu^{el}$ includes both the elastic energy density at the surface μ^{el}, and the capillary potential $\mu^s = -\gamma\,\Delta_S h$ with the surface energy γ. In units of the space scale $l_0 = \gamma/[2(1+\nu)\mathcal{E}_0]$ and timescale $t_0 = l_0^4/D\gamma$, the solution of the evolution equation reads in Fourier space

$$\hat{h}_1(\boldsymbol{k}, t) = e^{\sigma_{\boldsymbol{k}} t}\,\hat{h}_1(\boldsymbol{k}, 0) \quad \text{with} \quad \sigma_{\boldsymbol{k}} = c_3(\boldsymbol{k})\,k^3 - k^4. \quad (9)$$

The anisotropy of the strain relaxation enforces the anisotropy of the growth rate $\sigma_{\boldsymbol{k}}$. We plot in Fig. 6, $\sigma_{\boldsymbol{k}}$ for typical values of η. It exhibits maxima clearly localized around the k_y axis even for a small anisotropy $\eta = 0.8$, as opposed to the symmetric case $\eta = 1$. Consequently, the evolution of the surface is strongly anisotropic. We plot in Fig. 7 a typical example of the evolution predicted by Eq. (9) with the asymmetry parameter

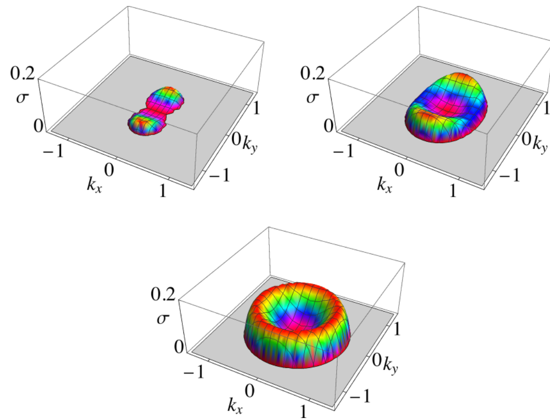

FIG. 6. Growth rate $\sigma_{\mathbf{k}}$ of the asymmetric ATG instability as a function of the wave-vector components. The plot corresponds to values of the asymmetry parameter of (left) experimental value on a 10° off vicinal surface $\eta = 0.36$, (middle) $\eta = 0.8$, and (right) symmetric case $\eta = 1$. Negative values that correspond to inhibited modes are not displayed.

$\eta = 0.36$ and for a peak to peak amplitude of 4 nm that correspond to the experiments displayed above for a vicinal substrate. The resulting asymmetric instability does indeed describe an elongation in the direction perpendicular to the steps, as found in experiments. It may be rationalized by the fact that the instability is driven by strain, that is partially relaxed perpendicularly to the steps, but not along them. Even with the partial relaxation measured experimentally, the morphology already exhibits a strong elongation perpendicular to the steps. It is also noticeable that the morphologies exhibited by experiments and theory look similar, with fingerlike patterns, Fig. 7.

C. Quantitative comparison

Beyond the qualitative morphological comparison between the experimental and theoretical finding, we now turn to their quantitative correspondence, see Fig. 7. The experiments are done with the parameters given above, and Fig. 7 corresponds to a corrugation with a peak to peak amplitude of 4 nm. For the analytical solution (9), we set parameters typical of a $Si_{1-x}Ge_x$film on Si(001), see, e.g., Ref. [44], with $x = 0.23$. In addition, in order to set the length scale l_0, we use the comparison between the experimental and theoretical Fourier spectra on a nominal substrate. We find experimentally the instability wavelength $\lambda_{\text{ATG}} = 2\pi/\sqrt{\langle k^2\rangle} = 127$ nm. To get theoretically the same wavelength on a nominal substrate, we set $l_0 = 15.2$ nm. For asymmetric systems, we consider the asymmetry measured experimentally $\eta \simeq 0.36$ for a 10° vicinal substrate. The initial surface is given by a white noise with an amplitude of 0.1 nm, as measured experimentally. We integrate the evolution equation up to a final amplitude of 4 nm also, see Fig. 7.[1]

[1]We choose this procedure instead of the use of the experimental growth duration given the large uncertainty in the diffusion coefficient that enters in the timescale t_0.

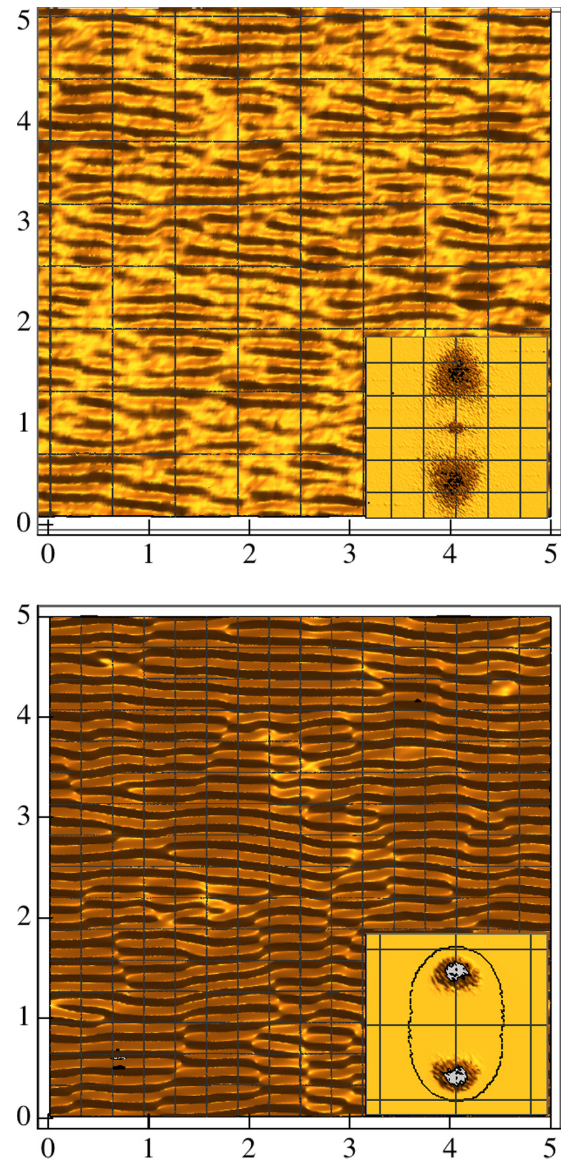

FIG. 7. (Left) Large-scale AFM image of the growth on a 10° off substrate for a composition $x = 0.23$. (Right) Integration of the evolution equation (9) with an in-plane asymmetry $\eta = 0.36$. In both images, distances are given in micrometers.

First, we compute the typical wavelength along y, $\lambda_y^{\text{th}} = 2\pi/\sqrt{\langle k_y^2\rangle}$ and find $\lambda_y^{\text{th}} = 11.5$ in dimensionless units, that corresponds to 174 nm with l_0 given above. This value is quite close to the experimental one $\lambda_y^{\text{exp}} = 204$ nm especially given all the approximations made in the model. Interestingly, we find that the instability wavelength in the vicinal/asymmetric case is larger than on the nominal case, $\lambda_y^{\text{exp}}/\lambda_{\text{ATG}} = 1.6$, while $\lambda_y^{\text{th}}/\lambda_{\text{ATG}} = 1.4$. This increase in the instability wavelength is related to the overall decrease in the mean strain that necessarily leads to an increase in the wavelength, that inversely depends on the mean strain.

Second, we also characterize the asymmetry of the resulting elongation by looking at the x and y properties. We may again define a typical length scale along x, $\lambda_x^{\text{th}} = 2\pi/\sqrt{\langle k_x^2\rangle}$. We find experimentally $\lambda_x^{\text{exp}} = 830$ nm, while theoretically,

$\lambda_x = 86.5$ in dimensionless units, that translates to 1300 nm with l_0 given above. The asymmetry ratio λ_x/λ_y is 4.0 experimentally and 7.5 theoretically. The comparison in the x direction is overall satisfactory given the large uncertainty in the calculation of λ_x and shape of the Fourier spectra. Note that the instability leads to ripples that can extend up to 2 μm following their undulations.

VI. CONCLUSION

We have shown both theoretically and experimentally that an in-plane relaxation anisotropy or equivalent misfit anisotropy allows to fabricate planar SiGe 1D elongations. Such situation is met during SiGe heteroepitaxy on vicinal Si substrate where steps induce strain relaxation in the direction perpendicular to their edges. When misorientation is sufficiently high, SiGe forms nanowires that self-assemble into nice periodic networks whose lengths extend perpendicularly to the step edges over mean distances up to 2 μm. Both qualitative and quantitative comparisons show that the rationalisation of the experimental finding can be done within the description of the ATG instability in presence of an in-plane strain anisotropy as measured by x-ray diffraction. Further investigation of the extension of the instability length and width as a function of the miscut angle, and hence of the strain anisotropy, is under consideration, together with extension to other epitaxial systems.

ACKNOWLEDGMENT

The authors would like to thank the CSC fellowship program.

[1] C. J. Moore, C. M. Retford, M. J. Beck, M. Asta, M. J. Miksis, and P. W. Voorhees, Orientation Dependence of Strained-Ge Surface Energies near (001): Role of Dimer-Vacancy Lines and Their Interactions with Steps, Phys. Rev. Lett. **96**, 126101 (2006).

[2] T. U. Schülli, G. Vastola, M.-I. Richard, A. Malachias, G. Renaud, F. Uhlík, F. Montalenti, G. Chen, L. Miglio, F. Schäffler, and G. Bauer, Enhanced Relaxation and Intermixing in Ge Islands Grown on Pit-Patterned Si(001) Substrates, Phys. Rev. Lett. **102**, 025502 (2009).

[3] G. Vastola, V. B. Shenoy, J. Guo, and Y.-W. Zhang, Coupled evolution of composition and morphology in a faceted three-dimensional quantum dot, Phys. Rev. B **84**, 035432 (2011).

[4] H. Hu, H. Gao, and F. Liu, Quantitative Model of Heterogeneous Nucleation and Growth of Sige Quantum dot Molecules, Phys. Rev. Lett. **109**, 106103 (2012).

[5] V. A. Zinovyev, A. V. Dvurechenskii, P. A. Kuchinskaya, and V. A. Armbrister, Strain-Induced Formation of Fourfold Symmetric Sige Quantum dot Molecules, Phys. Rev. Lett. **111**, 265501 (2013).

[6] J.-N. Aqua, I. Berbezier, L. Favre, T. Frisch, and A. Ronda, Growth and self-organization of SiGe nanostructures, Phys. Rep. **522**, 59 (2013).

[7] Y. Ma, S. Huang, C. Zeng, T. Zhou, Z. Zhong, T. Zhou, Y. Fan, X. Yang, J. Xia, and Z. Jiang, Towards controllable growth of self-assembled sige single and double quantum dot nanostructures, Nanoscale **6**, 3941 (2014).

[8] K. A. Lozovoy, A. P. Kokhanenko, and A. V. Voitsekhovskii, Influence of edge energy on modeling the growth kinetics of quantum dots, Cryst. Growth Des. **15**, 1055 (2015).

[9] N. Ares, G. Katsaros, V. N. Golovach, J. J. Zhang, A. Prager, L. I. Glazman, O. G. Schmidt, and S. De Franceschi, SiGe quantum dots for fast hole spin Rabi oscillations, Appl. Phys. Lett. **103**, 263113 (2013).

[10] M. Grydlik, M. T. Lusk, F. Hackl, A. Polimeni, T. Fromherz, W. Jantsch, F. Schäffler, and M. Brehm, Laser level scheme of self-interstitials in epitaxial Ge dots encapsulated in Si, Nano Lett. **16**, 6802 (2016).

[11] M. Grydlik, F. Hackl, H. Groiss, M. Glaser, A. Halilovic, T. Fromherz, W. Jantsch, F. Schäffler, and M. Brehm, Lasing from glassy Ge quantum dots in crystalline Si, ACS Photonics **3**, 298 (2016).

[12] S. A. Hafiz, R. J. A. Esteves, D. O. Demchenko, I. U. Arachchige, and Ü. Özgür, Energy gap tuning and carrier dynamics in colloidal gesn quantum dots, J. Phys. Chem. Lett. **7**, 3295 (2016).

[13] M. Abbarchi, M. Naffouti, B. Vial, A. Benkouider, L. Lermusiaux, L. Favre, A. Ronda, S. Bidault, I. Berbezier, and N. Bonod, Wafer scale formation of monocrystalline silicon-based mie resonators via silicon-on-insulator dewetting, ACS Nano **8**, 11181 (2014).

[14] T. J. Knapp, R. T. Moh, Y. S. Li, T. Brandur, R. H. Foote, X. Wu, D. R. Ward, D. E. Savage, M. G. Lagally, M. Friesen, S. N. Coppersmith, and M. A. Eriksson, Characterization of a gate-defined double quantum dot in a Si/SiGe nanomembrane, Nanotechnol. **27**, 154002 (2016).

[15] A. Hubert, E. Nowak, K. Tachi, V. Maffini-Alvaro, C. Vizioz, C. Arvet, J.-P. Colonna, J.-M. Hartmann, V. Loup, L. Baud *et al.*, A stacked sonos technology, up to 4 levels and 6nm crystalline nanowires, with gate-all-around or independent gates (ϕ-flash), suitable for full 3d integration, in *2009 IEEE International Electron Devices Meeting (IEDM)* (IEEE, Montgomery Village, 2009), pp. 1–4.

[16] S. Gupta, V. Moroz, L. Smith, Q. Lu, and K. C. Saraswat, 7-nm FinFET CMOS design enabled by stress engineering using Si, Ge, and Sn, IEEE Transac. Elec. Dev. **61**, 1222 (2014).

[17] J.-B. Moon, D.-I. Moon, and Y.-K. Choi, A bandgap-engineered silicon-germanium biristor for low-voltage operation, IEEE Transac. Elec. Dev. **61**, 2 (2014).

[18] M. Amato, S. Ossicini, and R. Rurali, Band-offset driven efficiency of the doping of SiGe core–shell nanowires, Nano Lett. **11**, 594 (2011).

[19] L. Zhang, M. d'Avezac, J.-W. Luo, and A. Zunger, Genomic design of strong direct-gap optical transition in Si/Ge core/multishell nanowires, Nano Lett. **12**, 984 (2012).

[20] J. Wang, J.-W. Luo, L. Zhang, and A. Zunger, Reinterpretation of the expected electronic density of states of semiconductor nanowires, Nano Lett. **15**, 88 (2014).

[21] J. Greil, A. Lugstein, C. Zeiner, G. Strasser, and E. Bertagnolli, Tuning the electro-optical properties of germanium nanowires by tensile strain, Nano Lett. **12**, 6230 (2012).

[22] B.-H. Lee, M.-H. Kang, D.-C. Ahn, J.-Y. Park, T. Bang, S.-B. Jeon, J. Hur, D. Lee, and Y.-K. Choi, Vertically integrated multiple nanowire field effect transistor, Nano Lett. **15**, 8056 (2015).

[23] L. Chen, F. Cai, U. Otuonye, and W. D. Lu, Vertical Ge/Si core/shell nanowire junctionless transistor, Nano Lett. **16**, 420 (2015).

[24] G. Zheng, W. Lu, S. Jin, and C. M. Lieber, Synthesis and fabrication of high-performance n-type silicon nanowire transistors, Adv. Mat. **16**, 1890 (2004).

[25] J. Tatebayashi, S. Kako, J. Ho, Y. Ota, S. Iwamoto, and Y. Arakawa, Room-temperature lasing in a single nanowire with quantum dots, Nat. Photonics **9**, 501–505 (2015).

[26] J. W. Ma, W.-J. Lee, J. M. Bae, K.-S. Jeong, S. H. Oh, J. H. Kim, S.-H. Kim, J.-H. Seo, J.-P. Ahn, H. Kim *et al.*, Carrier mobility enhancement of tensile strained Si and SiGe nanowires via surface defect engineering, Nano Lett. **15**, 7204 (2015).

[27] T. David, K. Liu, A. Ronda, L. Favre, M. Abbarchi, M. Gailhanou, P. Gentile, D. Buttard, V. Calvo, M. Amato, J.-N. Aqua, and I. Berbezier, Tailoring strain and morphology of core–shell SiGe nanowires by low-temperature Ge condensation, Nano Lett. **17**, 7299 (2017).

[28] F. C. Lang, Y. R. Zhao, Y. M. Xing, F. Liu, X. H. Hou, J. Zhu, J. J. Li, and S. T. Yang, A novel raster-scanning method to fabricate ultra-fine cross-gratings for the generation of electron beam moiré fringe patterns, Optics Lasers Eng. **86**, 281–290 (2016).

[29] P. D. Szkutnik, A. Sgarlata, A. Balzarotti, N. Motta, A. Ronda, and I. Berbezier, Early stage of Ge growth on Si(001) vicinal surfaces with an 8° miscut along [110], Phys. Rev. B **75**, 033305 (2007).

[30] L. Persichetti, A. Sgarlata, M. Fanfoni, and A. Balzarotti, Shaping Ge Islands on Si(001) Surfaces with Misorientation Angle, Phys. Rev. Lett. **104**, 036104 (2010).

[31] B. Sanduijav, D. Scopece, D. Matei, G. Chen, F. Schäffler, L. Miglio, and G. Springholz, One-Dimensional to Three-Dimensional Ripple-to-Dome Transition for SiGe on Vicinal Si (1 1 10), Phys. Rev. Lett. **109**, 025505 (2012).

[32] I. Berbezier, B. Gallas, L. Lapena, J. Fernandez, J. Derrien, and B. Joyce, New insights on SiGe growth instabilities, J. Vac. Sci. Technol. B **16**, 1582 (1998).

[33] I. Berbezier, A. Ronda, and A. Portavoce, SiGe nanostructures: new insights into growth processes, J. Phys. : Condens. Matter **14**, 8283 (2002).

[34] R. J. Asaro and W. A. Tiller, Interface morphology developpment during stress-corrosion cracking: Part 1. Via surface diffusion, Metall. Trans. **3**, 1789 (1972).

[35] M. A. Grinfeld, Instability of the separation boundary between a nonhydrostatiscally stressed elastic body and a melt, Sov. Phys. Dokl. **31**, 831 (1986).

[36] J.-N. Aqua, A. Gouyé, A. Ronda, T. Frisch, and I. Berbezier, Interrupted Self-Organization of SiGe Pyramids, Phys. Rev. Lett. **110**, 096101 (2013).

[37] C. Duport, P. Nozières, and J. Villain, New Instability in Molecular Beam Epitaxy, Phys. Rev. Lett. **74**, 134 (1995).

[38] J. Tersoff, Y. H. Phang, Z. Zhang, and M. G. Lagally, Step-Bunching Instability of Vicinal Surfaces Under Stress, Phys. Rev. Lett. **75**, 2730 (1995).

[39] Y. Xiang, Derivation of a continuum model for epitaxial growth with elasticity on vicinal surface, SIAM Journal on Applied Mathematics, SIAM J. Appl. Math. **63**, 241 (2002).

[40] L. Landau and E. Lifchitz, *Theory of Elasticity* (USSR Academy of Sciences, Moscow, USSR, 1986).

[41] J. N. Aqua and X. Xu, Directed self-organization of quantum dots, Phys. Rev. E **90**, 030402 (2014).

[42] T. David, J.-N. Aqua, K. Liu, L. Favre, A. Ronda, M. Abbarchi, J.-B. Claude, and I. Berbezier, New strategies for producing defect free sige strained nanolayers, Sci. Rep. **8**, 2891 (2018).

[43] J.-N. Aqua, T. Frisch, and A. Verga, Nonlinear evolution of a morphological instability in a strained epitaxial film, Phys. Rev. B **76**, 165319 (2007).

[44] J.-N. Aqua and T. Frisch, Influence of surface energy anisotropy on the dynamics of quantum dot growth, Phys. Rev. B **82**, 085322 (2010).

[45] K. Liu, I. Berbezier, T. David, L. Favre, A. Ronda, M. Abbarchi, P. Voorhees, and J.-N. Aqua, Nucleation versus instability race in strained films, Phys. Rev. Matt. **1**, 053402 (2017).

[46] H.-C. Jeong and E. D. Williams, Steps on surfaces: experiment and theory, Surf. Sci. Rep. **34**, 171 (1999).

[47] C. Misbah, O. Pierre-Louis, and Y. Saito, Crystal surfaces in and out of equilibrium: A modern view, Rev. Mod. Phys. **82**, 981 (2010).

[48] J.-N. Aqua, A. Gouyé, T. Auphan, T. Frisch, A. Ronda, and I. Berbezier, Orientation dependence of the elastic instability on strained SiGe films, Appl. Phys. Lett. **98**, 161909 (2011).

[49] H. J. W. Zandvliet, Energetics of si(001), Rev. Mod. Phys. **72**, 593 (2000).

[50] W. W. Mullins, Theory of thermal grooving, J. Appl. Phys. **28**, 333 (1957).

[51] B. J. Spencer, P. W. Voorhees, and S. H. Davis, Morphological Instability in Epitaxially Strained Dislocation-Free Solid Films, Phys. Rev. Lett. **67**, 3696 (1991).